SUPPORTING INFORMATION

Optically Active Defects in Carbon Nanotubes via Chlorination: Computational Insights

Braden M. Weight,[1,2] Brendan J. Gifford,[1,3] Grace Tiffany,[1] Elva Henderson,[1,4] Deyan Mihaylov,[5] Dmitri Kilin,[a] and Svetlana Kilina[1*]

[1]*Department of Chemistry and Biochemistry, North Dakota State University, Fargo, North Dakota 58108, U.S.A*
[2]*Department of Physics and Astronomy, University of Rochester, Rochester, NY 14627, U.S.A*
[3]*Center for Integrated Nanotechnologies, Materials Physics and Applications Division, Los Alamos National Laboratory, Los Alamos, New Mexico 87545, U.S.A.*
[4]*University of Pittsburgh, Pittsburgh, PA 15260, U.S.A.*
[5]*Theory Division, Laboratory for Laser Energetics, University of Rochester, Rochester, NY 14627, U.S.A*

Benchmarking of Methodology for the Ground State Calculations. Differences between trends of the adduct-SWCNT binding energies and geometries of 2-unit systems as calculated with different functionals are marginal, as can be seen in **Figs S1** and **S2**. The strongest binding is observed for the PBE functional (**Fig. S1a**, **c**). Introducing the Hartree-Fock exchange (HFE) weakens the binding by about 0.4 eV but only results in slight changes to the geometries (**Fig. S2a**, **c**). This suggests that adduct-SWCNT binding is artificially increased in these calculations, a phenomenon that has been previously described for PBE functional in aromatic systems.[1] The use of hybrid functionals reduces over-binding. Going from 20% HFE in B3LYP to 25% HFE in PBE1 results in significantly shortened C-Cl bond lengths (**Fig. S2a**, **c**) and the corresponding stronger binding between the SWCNT and Cl adducts (**Fig. S1a**, **c**). This stronger binding evidences the sp^3-hybridization of the carbon atom on the SWCNT adjacent to functionalization. The sp^2-hybridization of the pristine system is disrupted changing to the sp^3-hybridization in the vicinity of the functional group, leading to an increase in the bond length alternation (BLA), as observed in **Fig. S2a** and **c**. This effect is slightly intensified when wB97XD functional is used. Overall, the hybrid PBE1 functional provides the binding energies, the C-Cl bond length, and the C-C BLA comparable to the more advanced range-separated wB97XD functional that includes

dispersion corrections. This similarity is the most pronounced for neutral systems. Thus, we conclude that PBE1 provides more reasonable results, compared to B3LYP, which underestimates the binding energy and elongates the C-Cl bond, and PBE that overestimates the binding energies, while also elongates the C-Cl bond. While ωB97XD is expected to be more accurate for adduct-SWCNT interactions, it provides unreasonably large band gaps in optimized systems. Therefore, we have used PBE1 functional for benchmarking of different basis sets.

As with density functionals, using different basis sets results in generally similar qualitative trends for all chlorinated confirmations, as shown in **Figs S1b**, **d** and **S2b**, **d**. Increasing the basis set from STO-3G to 6-31G significantly reduce the strength of Cl-SWCNT binding (**Fig. S1b**, **d**), as well as the sp^3 character for the carbon atoms bonded to the chlorine in the system, as evidenced by the elongation of C-Cl bond lengths and decreasing C-C BLA within the hexagonal lattice (**Fig. S2b**, **d**). Inclusion of polarization functions to the basis set, stabilizes the energy of the system resulting in reasonably reduced C-Cl bond length and increased C-C BLA elucidating significant sp^3-character of carbon atoms involved in functionalization, compared to calculations using 6-31G basis set. The C-Cl bond lengths of 1.83-1.87 Å obtained by 6-31G* basis set are well agree with previous calculations of chlorinated zigzag and armchair SWCNTs of similar diameter to (6,2) SWCNT, calculated with the periodic boundary conditions (PBC) mimicking the infinite-length systems. As such, 6-31G* basis set is chosen for all further computations.

We would like to note that chlorinated (6,2) SWCNTs calculated with PBE functional and 6-31G* using PBC mimicking the infinite-length systems (**Fig. 1a**) exhibit a consistent stabilization of ~0.3 eV across all species likely due to the higher electron confinement in the finite systems. However, the general trend of both binding energies as well as geometries of neutral chlorinated SWCNTs calculated with PBC versus the finite tubes calculated with PBE1 and 6-31G* is in complete agreement (**Fig. S1a**). This indicates the length and capping schemes of the

finite systems is sufficient to accurately approximate their infinite counterparts, at least as qualitative trends are concerned.
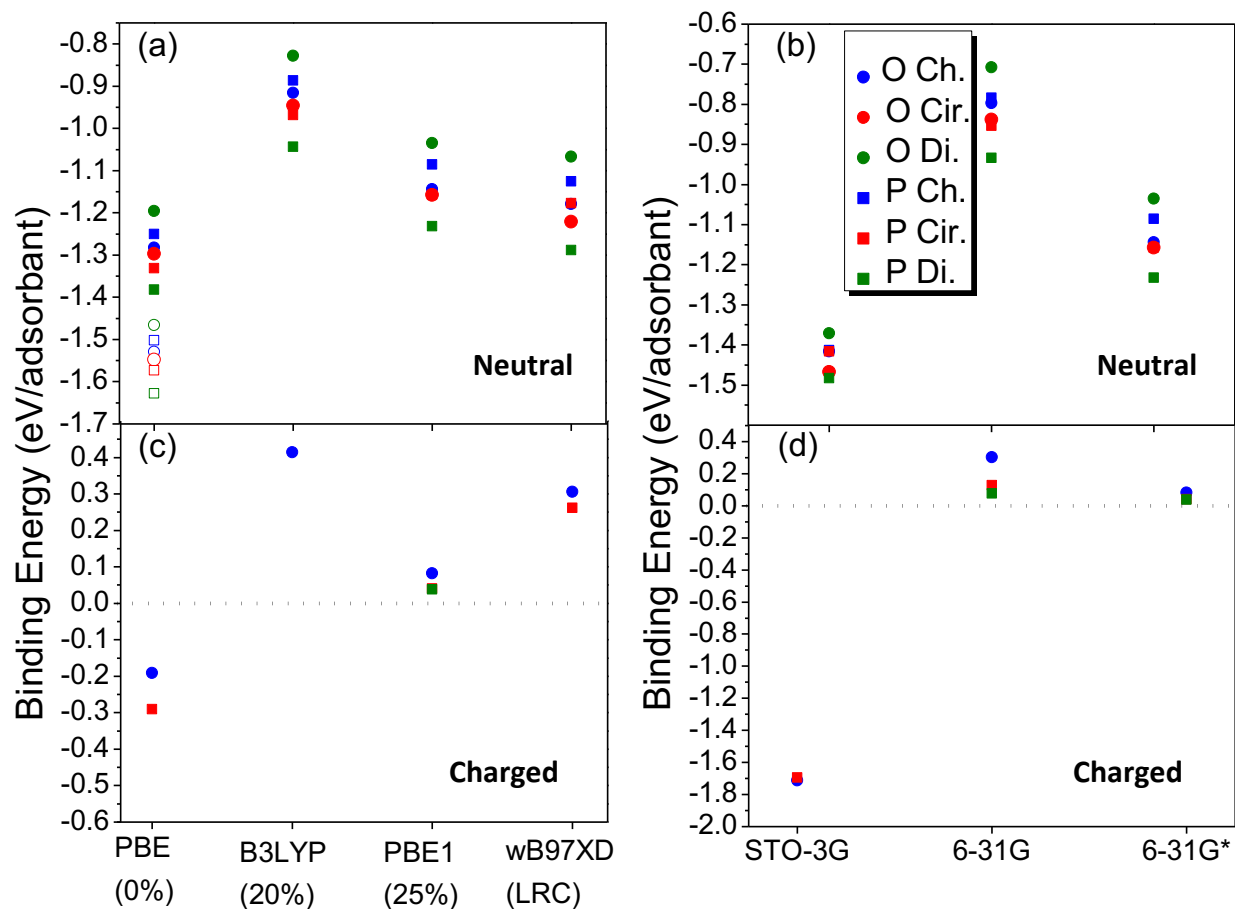

Figure S1: Comparison of binding energies of Cl to (6,2) SWCNT calculated by different methodologies. The data obtained by different density functionals (**a** and **c** panels) was computed with the basis set of 6-31G*. The data obtained by different basis sets (**b** and **d** panels) was computed with PBE1 functional consistently. Solid points indicate data for finite nanotubes of 2 units in length, whereas hollow points indicate the data from relevant calculations with periodic boundary conditions (PBC) to mimic infinitely long nanotubes. Panels (**a**) and (**b**) are for neutral systems, and panels (**c**) and (**d**) are present data from systems with a negative charge (-1 charge per each Cl adduct).
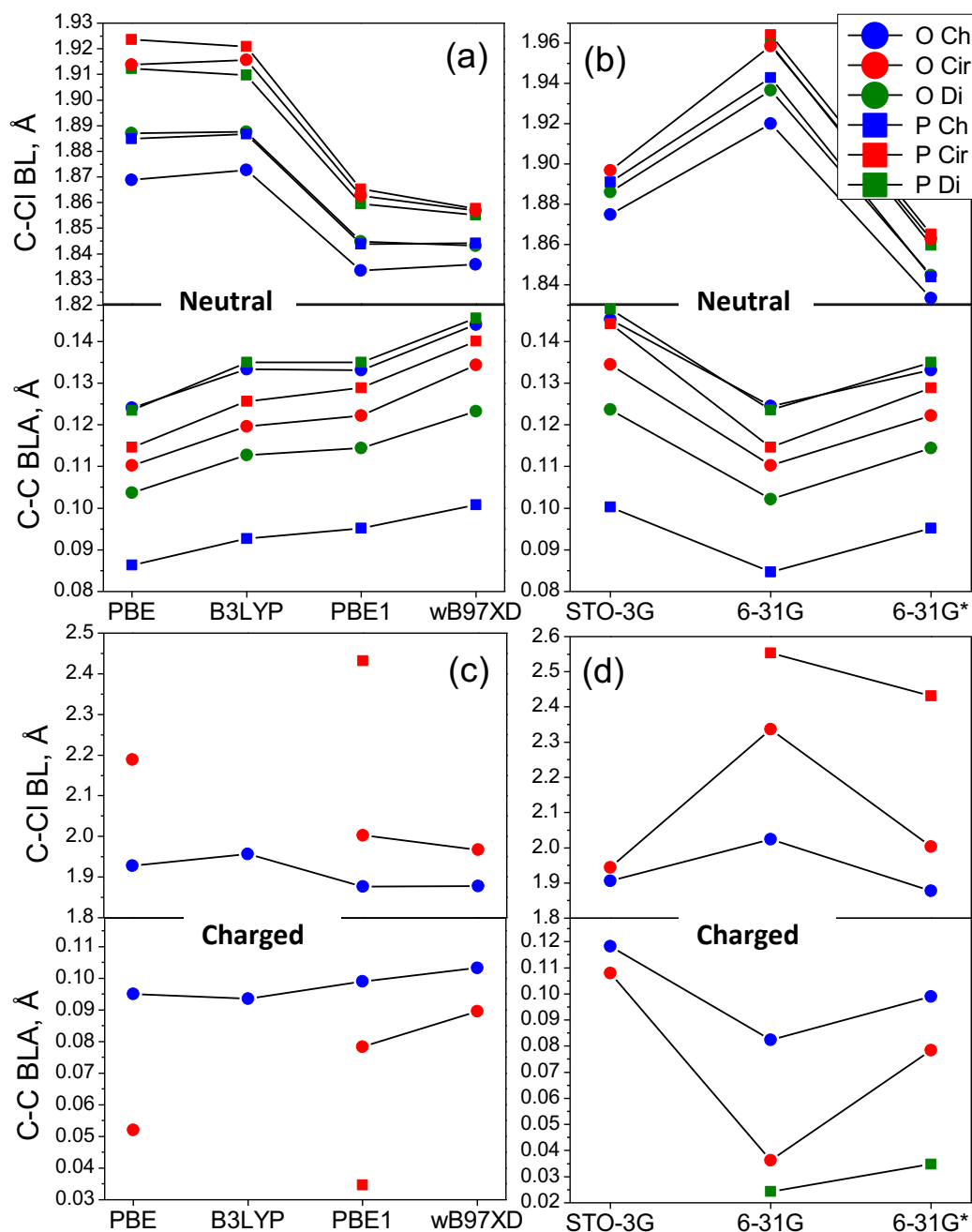
Figure S2: Bond character at the sp³-defect site of chlorinated (6,2) nanotubes of 2 units in size calculated using different methodologies. The upper part of each panel shows the average C-Cl bond length (BL), and the lower part shows the C-C bond length alternation (BLA). BLA is the average difference between the C-C bonds adjacent to the chlorine defect, which are expected to be elongated, and C-C bonds two bonds away from the chlorine defect, which are expected to be shortened. Panels (**a**) and (**b**) describe neutral nanotubes, while panels (**c**) and (**d**) describe charged tubes. Panels (**a**) and (**c**) show how the bond character changes with different functionals, all optimized with a 6-31G* basis set. Panels (**b**) and (**d**) show the bond character changes with different basis sets, all optimized with PBE1 functional.
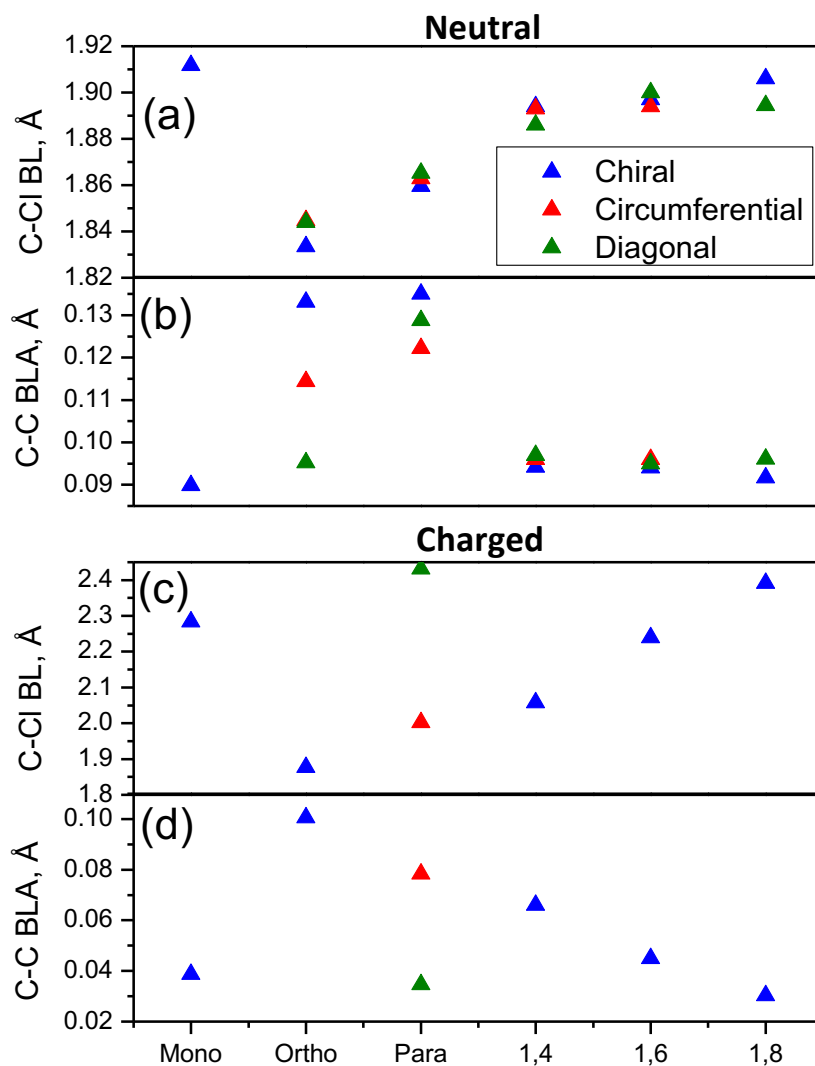
Figure S3: Bond length data for all 2-unit chlorinated finite (6,2) nanotube arrangements optimized with PBE1 functional and 6-31G* basis set. Panels (**a**) and (**b**) describe the bond character of neutral chlorinated SWCNTs, while panels (**c**) and (**d**) describe the bond character of charged chlorinated SWCNTs. Panels (**a**) and (**c**) show the C-Cl bond length (BL) with respect to the Cl arrangement, and panels (**b**) and (**d**) show the C-C bond length alternation (BAL) with respect to the Cl arrangement. BLA is the average difference between the C-C bonds adjacent to the chlorine defect, which are expected to be elongated, and C-C bonds two bonds away from the chlorine defect, which are expected to be shortened.

For neutral cases, the bond lengths for arrangements where Cl are bonded to different rings are similar to the monochlorinated case, while cases where Cl are bonded to the same ring show much smaller C-Cl bonds and generally much greater bond length alternation. For charged cases, a similar trend appears, where dichlorinated cases become more like monochlorinated case as the Cl separation increases. The main outlier is the diagonal *para* arrangement, which shows much weaker bonding than other arrangements with two Cl atoms bonded to the same ring.
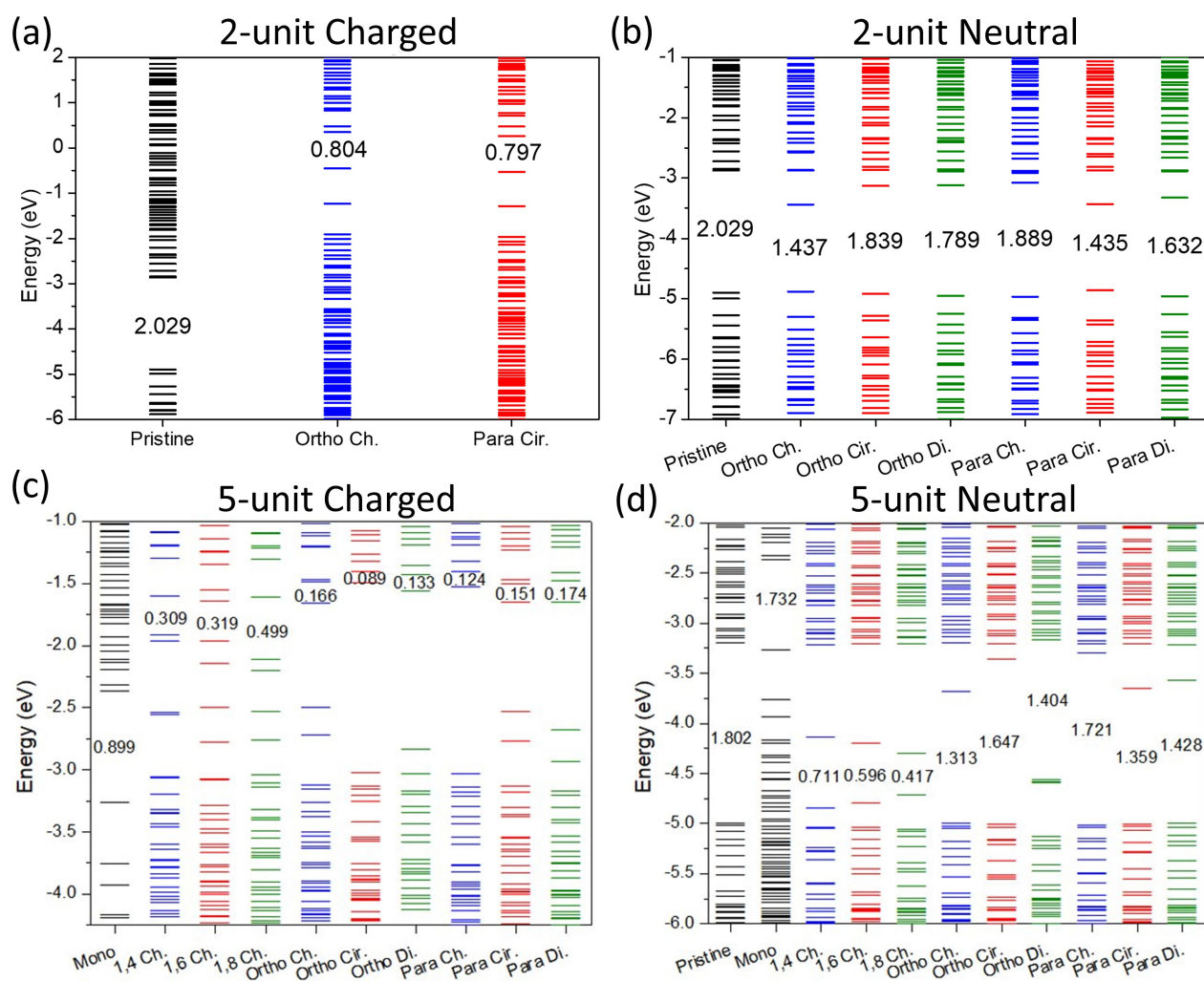
Figure S4: Molecular orbital diagram for chlorine doped SWCNTs calculated using PBE1 functional and 6-31G* basis set. The number in each diagram indicates the band gap for each arrangement. The character of p-doping is clearly observed for neutral chiral *ortho* and circumferential and diagonal *para* configurations. The character of n-doping is clearly observed in all charged cases. This is consistent in both the long systems (5-unit SWCNT) and the short systems (2-unit SWCNT).
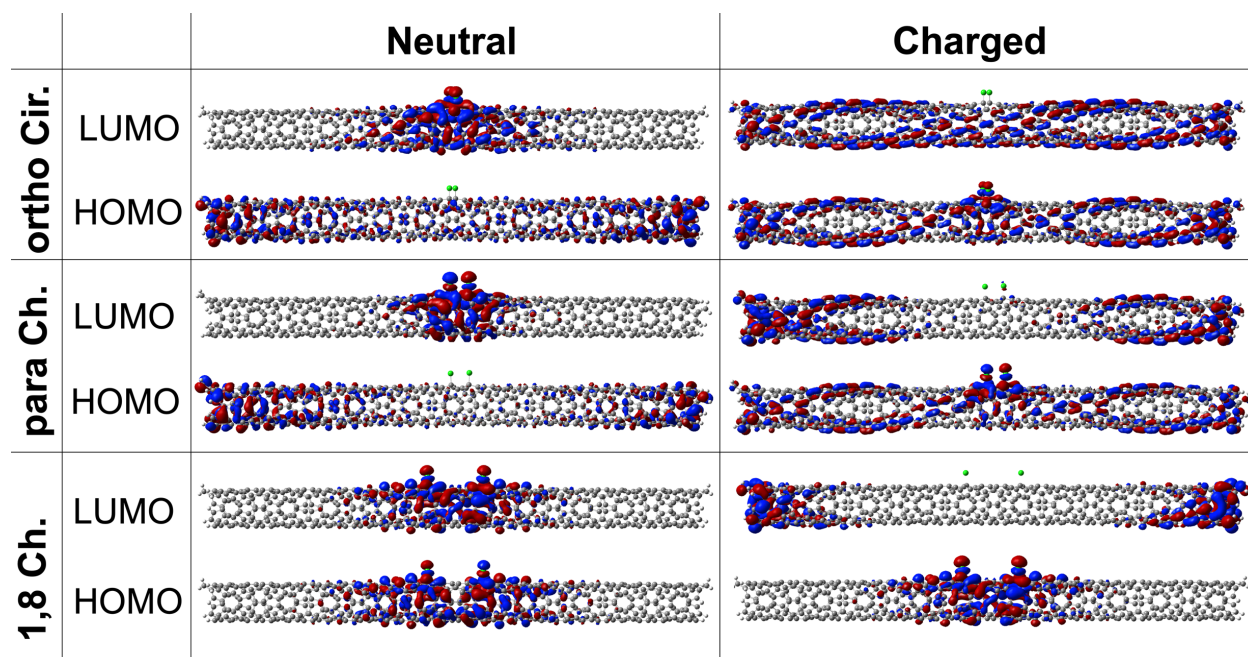
Figure S5: The calculated HOMO and LUMO for the *ortho* circumferential (Cir), *para* chiral (Ch.), and 1,8 chiral (Ch.) di-chlorinated schemes of the 5-unit cell (6,2) SWCNT model. The analogous HOMO and LUMO orbitals are shown in **Tables 1** and **2** in the main text for shorter 2-unit cell (6,2) model. For longer models, a smaller confinement effect reduces edge localization of frontier orbitals for charged systems with closely placed Cl adducts (*ortho* and *para* defects), compared to those of the shorter 2-unit SWCNT models (**Table 2** in the main text). However, for charged models with separated Cl adducts (like 1,8) the lowest unoccupied orbitals preserve their edge-localization character. This edge-localization is associated with a shallow character of the trap potential for this kind of defects, which is not deep enough to localize the charges in a presence of a strong Coulomb repulsion.
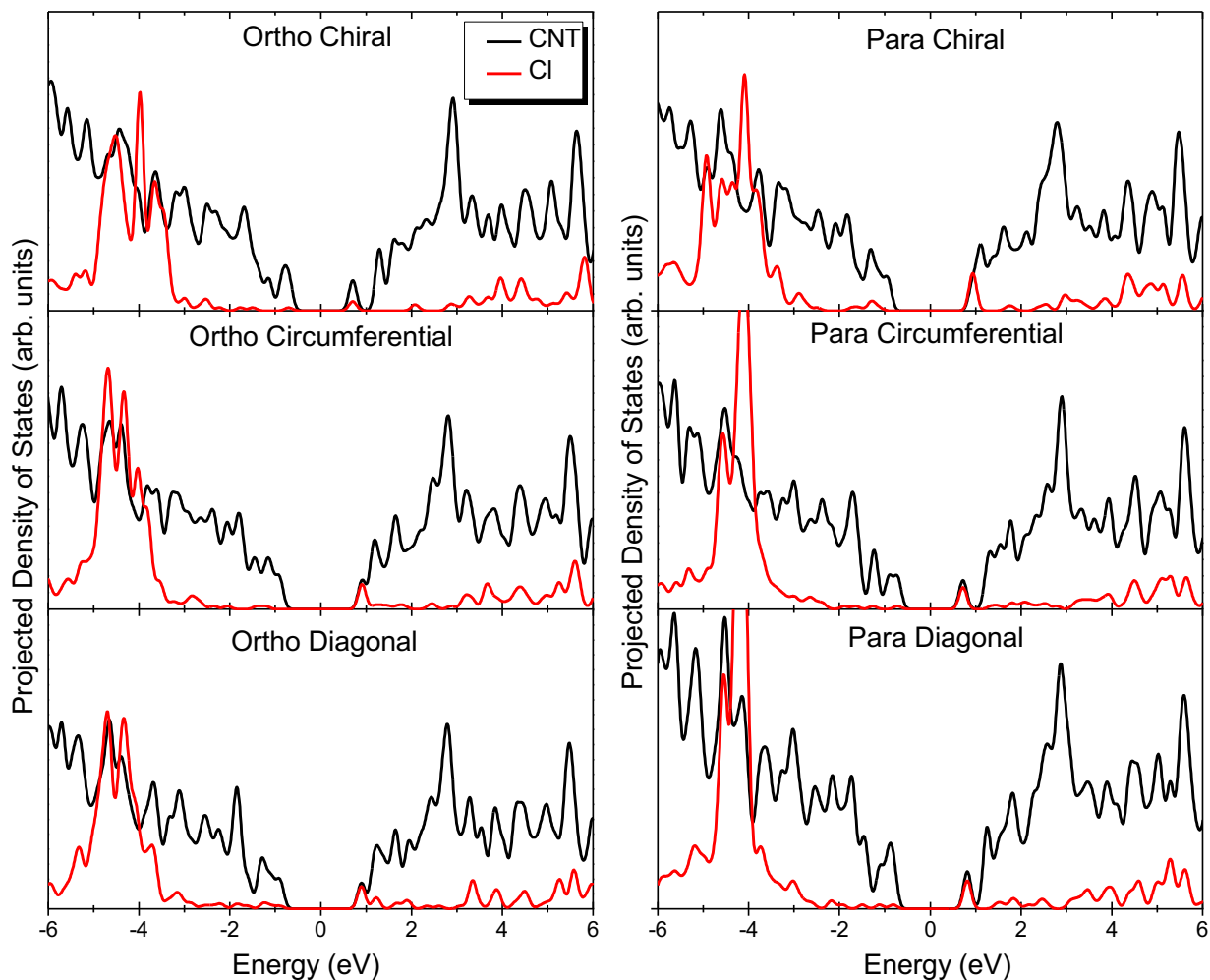
Figure S6: Projected density of states (PDOS) of *neutral* 2-unit in length (6,2) nanotubes with chlorines placed on the same carbon-ring of the nanotube at different configurations with respect to the tube axis. The PDOS of chlorines is multiplied by 10 for better visualization of chlorine contributions, compared to contributions of the much larger number of carbon atoms. The left panels are for *ortho* defects, and the right panels are for *para* defects. The zero energy is taken as the middle of the HOMO-LUMO gap of each system. For all configurations, the states at the edge of the conduction band, in particular, LUMO, originate from chlorines. The smallest energy gaps are observed for *ortho*-Chiral, *para*-Circumferential and *para*-Diagonal, when chlorine-originated state (LUMO) is well distinct from the edge of the conduction band. The HOMO has negligible contribution of chlorines for all cases.
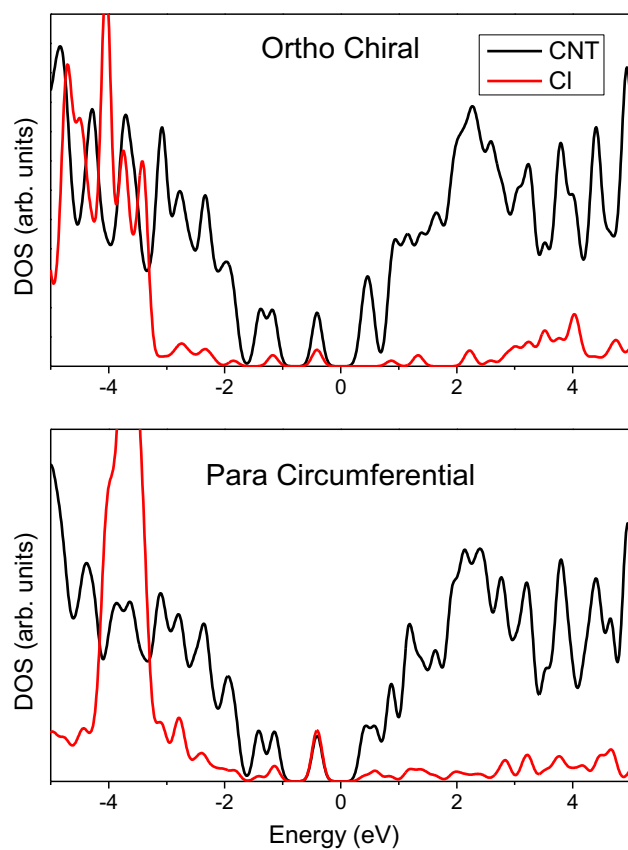
Figure S7: Projected density of states (PDOS) for *charged* finite (6,2) nanotubes of 2 units in length with chlorines placed on the same carbon-ring of the nanotube at the different configurations with respect to the tube axis. The PDOS of chlorines is multiplied by 10 for better visualization of chlorine contributions, compared to contributions of the much larger number of carbon atoms. The zero energy is taken as the middle of the HOMO-LUMO gap of each system. For both configurations, the states at the edge of the valence band, in particular, HOMO, have significant contribution of chlorines. For both systems, the LUMO shows much less contribution from chlorines.
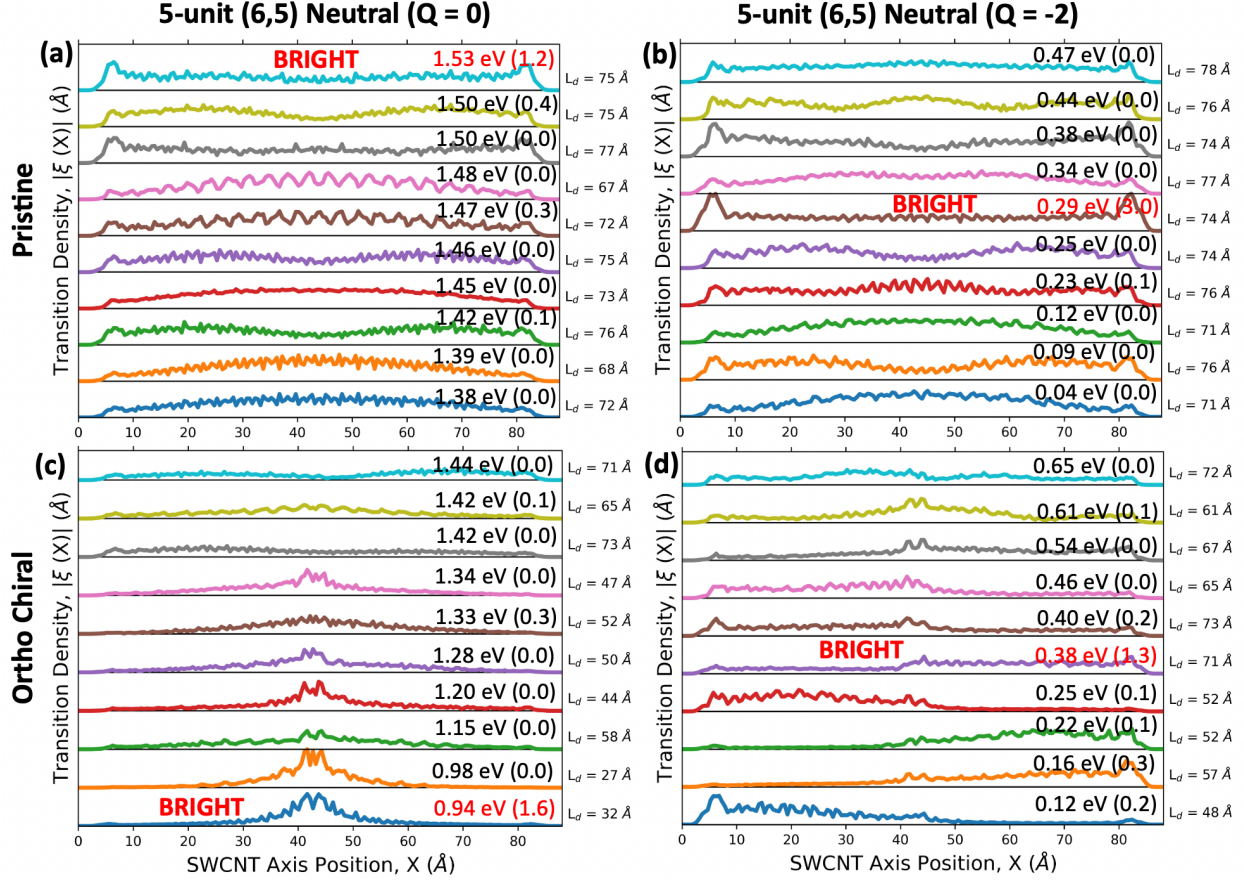
Figure S8: One-particle, ground-to-excited transition density,[2–5] projected along the nanotube axis for the 10 lowest-energy electronic transitions for 5-unit cell (6,2) SWCNT model with the *ortho* chiral defect and compared to the pristine system. (a) and (c) A neutral pristine and *ortho* chiral models, respectively; (b) and (d) charged pristine and *ortho* chiral models. The localization extent (i.e., the inverse participation ratio)[2,3,6,7] is shown for each transition, where a smaller L_d indicates a more localized exciton in units of Angstroms The energy and the oscillator strength (in prentices) of each exciton are also shown.

Figure S8 indicates that the introduction of charge leads to similar excitonic features as the neutral system. However, the low-energy states are more pristine-like due to the defect-localized HOMO orbital (see Table 4 in the main text) rather than delocalized as in the neutral case (see Table 3 in the main text). The localization length L_d, is defined as,

$$L_d = \frac{1}{\sum_n^{N_x}(P_n)^2}, \quad P_n = \frac{|\xi_{0\alpha}(X_n)|}{\sum_j^{N_x}|\xi_{0\alpha}(X_j)|}, \quad (1)$$

where $|\xi_{0\alpha}(X_n)|$ is the magnitude of the ground-to-α^{th} transition density at SWCNT axis X_n. Here, all of the transition density is summed into 0.5-Å bins along the SWCNT axis. P_n represents a probability distribution for the exciton, and L_d describes its localization across the real space histogram bins. The value is converted to a length as $L_d * 0.5$ Å → L_d for clarity.
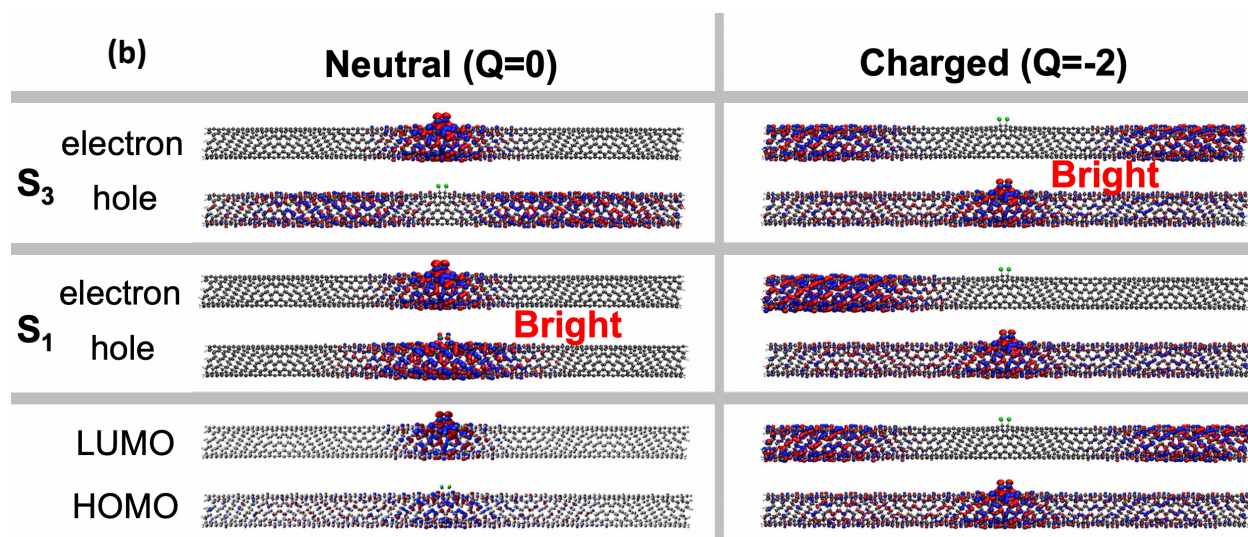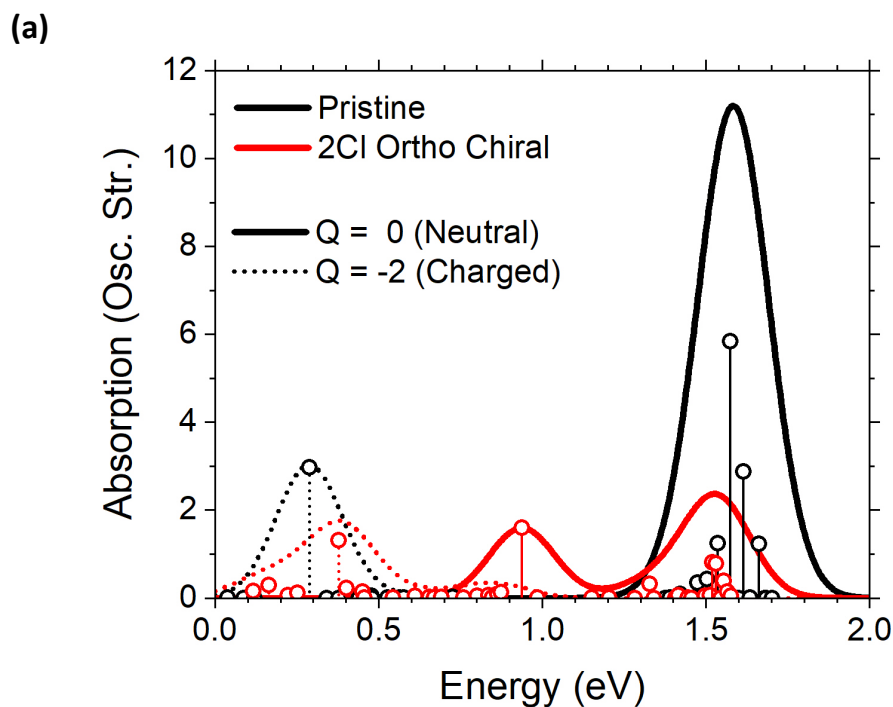
Figure S9: Optical properties for various 5-unit cell (6,5) SWCNT models. (a) Absorption spectra of Pristine (black) and *ortho* Chiral functionalized (red) systems with -2 charge (dashed lines) and neutral (solid lines). (b) the ground state HOMO and LUMO orbitals (S_0) and excited Natural Transition Orbitals representing the electron-hole pair contributing to the lower-energy excitonic states S_1 and S_3 for the neutral and charged *ortho* Chiral models.
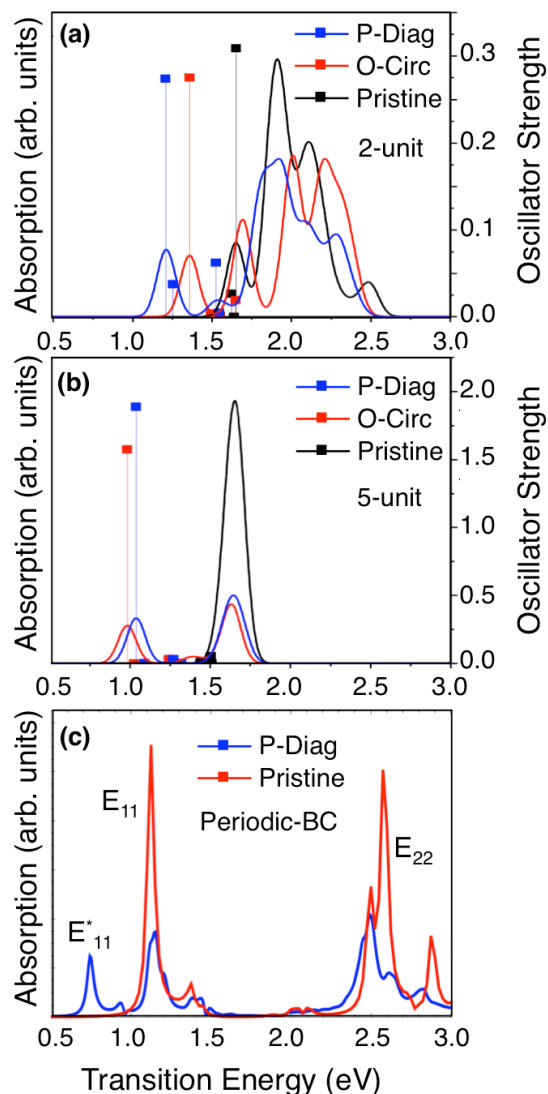
Figure S10: Absorption spectra of pristine and chlorinated neutral (6,2) SWCNTs with chlorines placed at the *ortho* (O) and *para* (P) positions along different directions with respect to the tube axis (diagonal (Diag) and circumferential (Circ)). The considered nanotubes are 2-unit **(a)** and 5-unit **(b)** in size and infinitely long simulated by inclusion of periodic boundary conditions (**c**). The finite-size tubes are calculated using TDDFT within the PBE0 functional and 6/31G* basis set, as implemented in Gausian-16 software package. The vertical lines in (a) and (b) identify the oscillator strength of four lowest-energy optical transitions for the finite-size systems. The infinitely long models in (c) are calculated based on Bethe–Salpeter equation (BSE) using the PBE0 functional and plane-wave basis set, implanted in VASP software, with the methodology details reported in Ref.[8] Increase in the nanotube length results in the redshift of the E^*_{11} defect-associated peak and the main E_{11} band coinciding with those of the pristine SWCNT. This redshift is a manifestation of the reduced confinement effect. Despite these differences, the optical spectra calculated by TDDFT and BSE methods are qualitatively comparable, justifying feasibility of the reduced finite-size models of SWCNTs. For all cases, the intensity the E_{11} band is significantly reduced as the result of functionalization, while the E^*_{11} defect-associated peak is redshifted and optically active. Note that BSE method allows for calculations not only the low-energy E_{11} band, but also the E_{22} band that is not computationally feasible with TDDFT due to much larger number of exited states required for simulations of higher energy spectral bands.
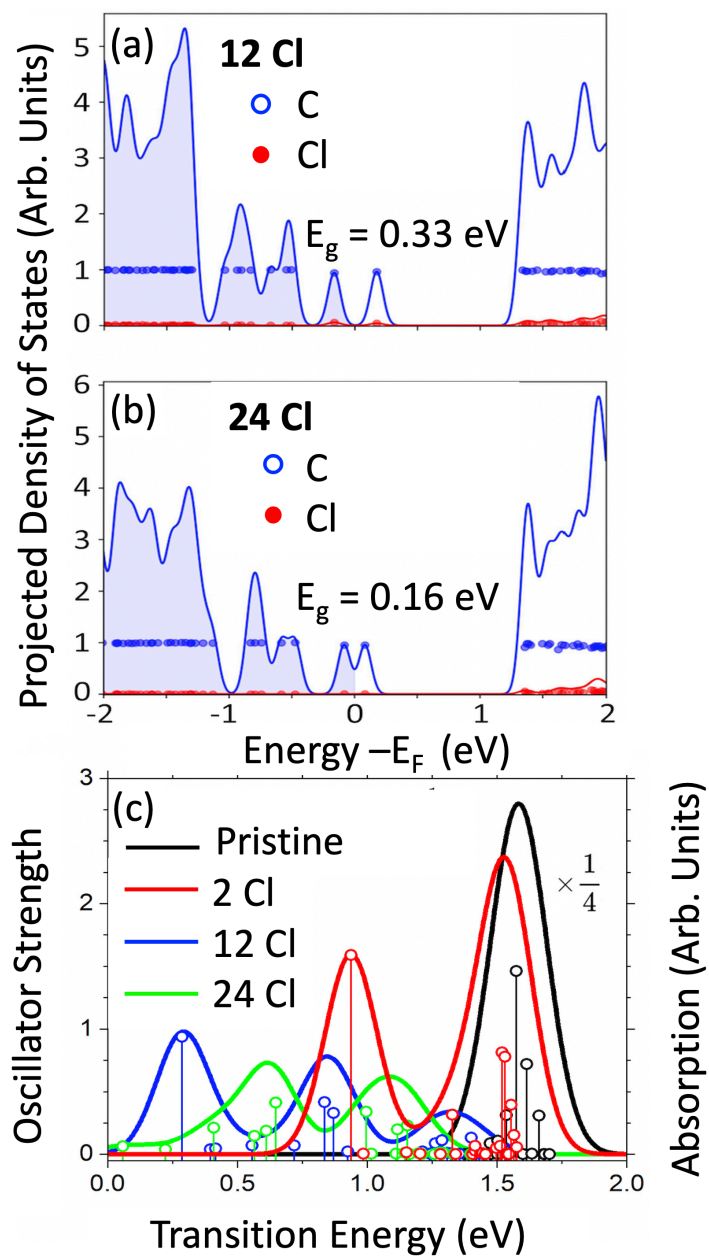
Figure S11: Concentration-dependent effects in neutral chlorine functionalization for the ground and excited electronic states of 5-unit cell (6,2) SWCNT. **(a)** and **(b)** The projected density of states for the SWCNT for different chlorine concentrations of 12 and 24 chlorin adducts, respectively, distributed at distances of 3-4 A° from each other to avoid interactions with the nanotube edges. The zero-value reference for the X-axis is taken as the middle of the HOMO-LUMO gap (E_f) for each model. **(c)** Simulated absorption spectra at various chlorine concentrations, compared to the spectra of the pristine SWCNT. The optical peak of the pristine system (black line) is reduced by 4 times for better visualization of optical peaks in chlorinated systems.

References

(1) Kilina, S.; Kilin, D.; Tretiak, S. Light-Driven and Phonon-Assisted Dynamics in Organic and Semiconductor Nanostructures. *Chem. Rev.* **2015**, *115* (12), 5929–5978. https://doi.org/10.1021/acs.chemrev.5b00012.

(2) Tretiak, S.; Mukamel, S. Density Matrix Analysis and Simulation of Electronic Excitations in Conjugated and Aggregated Molecules. *Chem. Rev.* **2002**, *102* (9), 3171–3212. https://doi.org/10.1021/cr0101252.

(3) Zheng, Y.; Weight, B. M.; Jones, A. C.; Chandrasekaran, V.; Gifford, B. J.; Tretiak, S.; Doorn, S. K.; Htoon, H. Photoluminescence Dynamics Defined by Exciton Trapping Potential of Coupled Defect States in DNA-Functionalized Carbon Nanotubes. *ACS Nano* **2021**, *15* (1), 923–933. https://doi.org/10.1021/acsnano.0c07544.

(4) Plasser, F.; Bäppler, S. A.; Wormit, M.; Dreuw, A. New Tools for the Systematic Analysis and Visualization of Electronic Excitations. II. Applications. *J. Chem. Phys.* **2014**, *141* (2), 024107. https://doi.org/10.1063/1.4885820.

(5) Plasser, F.; Wormit, M.; Dreuw, A. New Tools for the Systematic Analysis and Visualization of Electronic Excitations. I. Formalism. *J. Chem. Phys.* **2014**, *141* (2), 024106. https://doi.org/10.1063/1.4885819.

(6) Murphy, N. C.; Wortis, R.; Atkinson, W. A. Generalized Inverse Participation Ratio as a Possible Measure of Localization for Interacting Systems. *Phys. Rev. B* **2011**, *83* (18). https://doi.org/10.1103/PhysRevB.83.184206.

(7) Wegner, F. Inverse Participation Ratio in 2 + e Dimensions. *Z. Physik B Cond. Mat.* **1980**, *36* (3), 209–214. https://doi.org/10.1007/BF01325284.

(8) Kryjevski, A.; Mihaylov, D.; Gifford, B.; Kilin, D. Singlet Fission in Chiral Carbon Nanotubes: Density Functional Theory Based Computation. *The Journal of Chemical Physics* **2017**, *147* (3), 034106. https://doi.org/10.1063/1.4992785.